(FDR) < 0.01) included p53 signaling and cell cycle checkpoints, mRNA processing and the SWI/SNF complex (**Supplementary Fig. 13b** and **Supplementary Table 9**). *TP53* was mutated in only 3 cases (2.8%), but, considering these cases together with those with mutations in *ATM* ($n = 2$), *CHEK2* ($n = 1$), *MDM2* ($n = 1$) and *E2F3* ($n = 1$), copy number deletions in *CDKN2A* at 9p21 ($n = 17$; including 4 homodeletions) and gains in *MYC* at 8q24 ($n = 24$), a total of 42 cases (40%) had genetic alterations involved in p53 signaling and/or cell cycle checkpoints (**Fig. 5b**). The pathways involved in mRNA processing were not previously implicated in ccRCC. Frequent mutations in splicing machinery were reported in myelodysplastic syndromes (MDS) and in other hematopoietic neoplasms, with mutations affecting spliceosome components involved in recognizing the 3′ splice site[37]. In contrast, in ccRCC, mutated genes that were involved in mRNA processing were related to later steps in splicing, including the release of introns, 3′ end processing and mRNA export to the cytoplasm (**Supplementary Fig. 13c**).

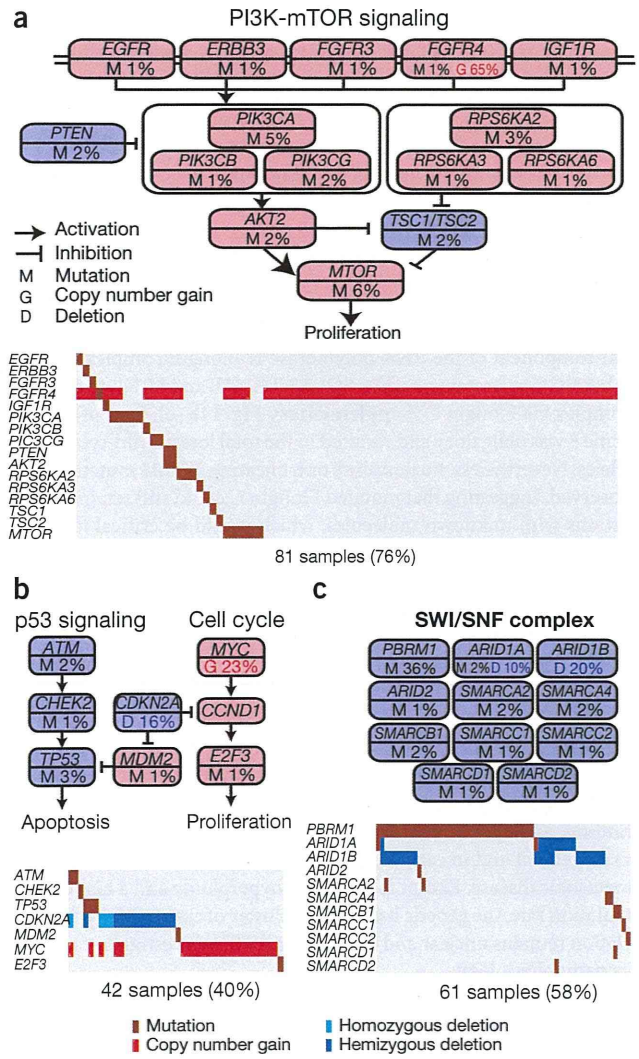

Figure 5 Significantly mutated pathways for 106 ccRCC specimens. (**a**–**c**) PI3K-mTOR signaling (**a**), p53 signaling (**b**) and the SWI/SNF complex (**c**) are commonly altered in ccRCC. Alterations are defined as somatic mutations and DNA copy number changes identified by GISTIC 2.0 analysis. Genes considered to be oncogenes or tumor suppressor genes are colored pink and blue, respectively.

PBRM1 was the second most commonly mutated gene in ccRCC and encodes a component of the SWI/SNF complex that regulates chromatin structure through ATP-dependent nucleosome remodeling. Other components of the SWI/SNF complex, including *ARID1A* and *ARID1B*, were within significantly deleted regions at 1p36 and 6q25, respectively. Taking into consideration these cases and those with mutations in *ARID1A* ($n = 2$), *SMARCA2* ($n = 2$), *SMARCA4* ($n = 2$), *SMARCB1* ($n = 2$) and other genes, a total of 61 cases (58%) had mutations and/or deletions in 11 different components of the SWI/SNF complex (**Fig. 5c**). These changes were not mutually exclusive, and 5 cases had ≥2 mutations. Multiple components of the SWI/SNF complex might be mutated in single cases in various types of cancer[38]. Notably, these five ccRCC cases had significantly worse prognosis compared to individuals with less than two mutations in the SWI/SNF complex (HR = 5.40, 95% CI = 1.56–14.5; $P = 0.0113$; Cox proportional hazards model), indicating that multiple mutations in the SWI/SNF complex could lead to aggressive phenotype in ccRCC.

Integrated molecular analysis of ccRCC

RNA sequencing was also performed in 100 ccRCC cases (**Supplementary Table 10**). In total, 44 fusion transcripts were identified in 25 specimens (**Supplementary Table 11**), of which about one-third ($n = 14$) were in frame. The lack of recurrent lesions largely obscured the significance of these fusions, except for *SETD2-QRICH1* and *NONO-TFE3* fusions. *TFE3* on Xp11 participates in promiscuous gene fusions with several partners, including *NONO*[39]. *TFE3*-containing fusions have been implicated in RCCs that are histologically distinct from typical ccRCCs (RCCs with Xp11 translocation)[39,40]. The current case with a *NONO-TFE3* fusion was positive for TFE3 expression in immunohistochemistry but showed histology otherwise indistinguishable from that typical for ccRCC cases[41] (**Supplementary Fig. 17**).

As previously reported, gene expression profiling of 101 ccRCC cases identified 2 major clusters—ccA and ccB—which were characterized by upregulated angiogenic factors and enhanced expression of genes involved in cell cycle progression, respectively (**Supplementary Fig. 18a–c**)[42]. In accordance with recent reports[10,20], Gene Set Enrichment Analysis (GSEA) showed discrete expression profiles in *BAP1*- and *PBRM1*-mutated tumors. *PBRM1*-mutated tumors were enriched for upregulated expression of the gene set with a hypoxia signature, whereas *BAP1*-mutated cases were associated with downregulated expression of target genes of polycomb repressive complex 2 (PRC2) (**Supplementary Fig. 19**).

DNA methylation profiling based on hierarchical clustering identified 3 distinct clusters that were characterized by different DNA methylation levels, including clusters with high, intermediate and low mean methylation levels, as determined using a total of 1,288 differentially methylated genes (**Fig. 6a, Online Methods** and **Supplementary Fig. 20**). Functional annotation analysis using The Database for Annotation, Visualization and Integrated Discovery (DAVID)[43] showed over-representation of homeobox genes in the 1,228 differentially methylated genes (**Supplementary Table 12**), and GSEA of the differentially methylated genes in the high and low-intermediate subgroups showed a marked enrichment in the cluster with high methylation of the gene set regulated by PRC2 and of the genes undergoing methylation at histone H3 lysine 27 (H3K27) (**Fig. 6b**). The cluster with high methylation was also characterized by a higher *BAP1* mutation rate ($P = 5.22 \times 10^{-3}$) and lower *BAP1* ($P = 2.11 \times 10^{-2}$) and higher *EZH2* ($P = 1.57 \times 10^{-5}$) expression levels (**Fig. 6c,d**). Notably, *BAP1* mutation ($P = 4.86 \times 10^{-3}$), decreased *BAP1* expression ($P = 7.46 \times 10^{-3}$) and increased *EZH2* expression ($P = 8.10 \times 10^{-3}$) were shown to be significantly associated with increased methylation of PRC2 target genes (**Supplementary Fig. 21**). These

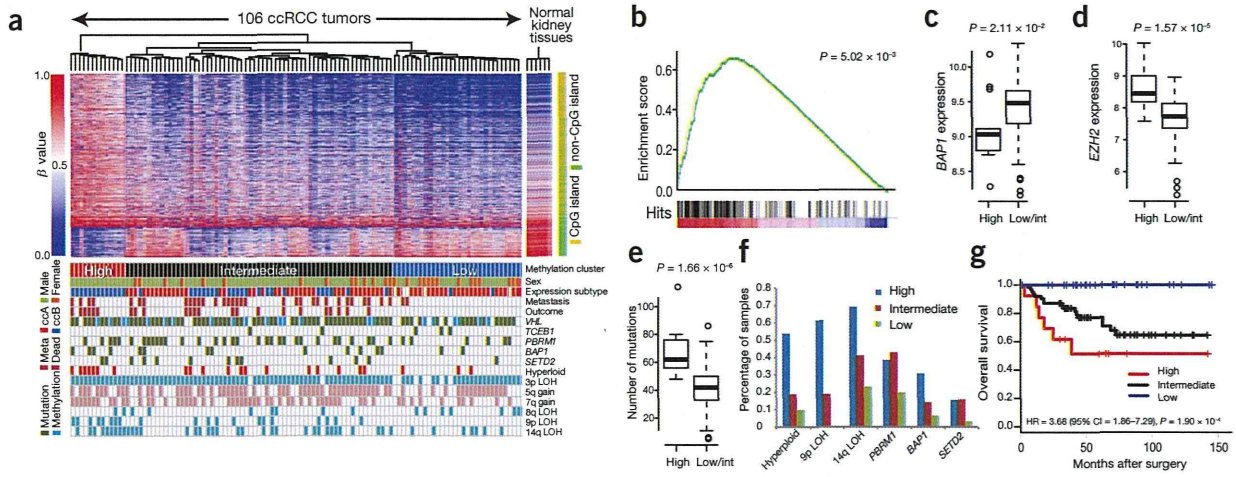

Figure 6 Correlations between DNA methylation and other genetic lesions. (**a**) Integrated view of DNA methylation clustering combined with mutation status of common driver genes, gene expression profiles and genome copy numbers. β values are for DNA methylation. Probes corresponding to CpG islands and non-CpG islands are shown on the right. Clinical outcomes and the presence-absence of metastasis are also shown. Meta, cases with distant metastasis. (**b**) GSEA showing significant enrichment of PRC2-regulated genes in differentially methylated genes in the subgroup with high DNA methylation. Hits displayed below the graph show where the members of the gene set appear in the ranked list of genes. (**c**–**g**) Integrated genetic and epigenetic analyses showed close correlation between DNA methylation status and *BAP1* expression (**c**), *EZH2* expression (**d**), total number of somatic mutations (**e**), hyperploidy, LOH at 9p, LOH at 14q and *PBRM1*, *BAP1* and *SETD2* mutations (**f**) and clinical outcome (**g**). *P* values were calculated using the *t* test in **c**–**e**, the Cochran-Armitage trend test in **f** and the log-rank test in **g**. Box plots show median, 25% and 75% quartile ranges.

findings strongly indicate that the cluster with high methylation was closely related to deregulated PRC2 activity.

Other prominent features of the cluster with high methylation included a higher number of somatic mutations ($P = 1.66 \times 10^{-6}$), more hyperploid cases ($P = 1.57 \times 10^{-3}$), cases with LOH at 14q ($P = 2.0 \times 10^{-4}$) and 9p ($P = 1.57 \times 10^{-3}$), enrichment of the ccB gene expression profile ($P = 2.46 \times 10^{-10}$) (**Fig. 6a,e,f**) and strong association with higher probability of metastasis (HR = 1.96, 95% CI = 1.17–3.30; $P = 1.11 \times 10^{-2}$) and poor overall survival (HR = 3.68, 95% CI = 1.86–7.29; $P = 1.90 \times 10^{-4}$) (**Fig. 6g**), which combined with the deregulated PRC2 profile, indicate that deregulation of polycomb-mediated gene silencing may contribute to aggressive tumor phenotype and poor clinical outcome.

DISCUSSION

Our comprehensive molecular study involving 106 ccRCC cases provided new insights into ccRCC genetics and biology and identified potential therapeutic targets. Similar to what has been observed in other cancers, the development of ccRCC seems to be shaped by the acquisition of a number of somatic gene mutations and chromosomal lesions that predominantly affect a handful of genes (*VHL*, *PBRM1*, *SETD2* and *BAP1*) and chromosome regions (3p, 5q, 9p and 14q), with many less frequent mutations additionally occurring in key targets. Pathway analysis of gene mutations disclosed several functional gene pathways, including PI3K-AKT-mTOR signaling, the KEAP1-NRF2 apparatus and mRNA processing, that were commonly affected by multiple, less frequent mutations.

A cardinal feature of ccRCC is a very high frequency of *VHL* inactivation caused by gene deletion, mutation and/or silencing via promoter methylation, leading to HIF accumulation. From this perspective, the discovery of *TCEB1* mutations and the obligatory loss of chromosome 8 in 36–42% of ccRCC cases with intact *VHL* was among the most notable findings of this study, demonstrating a new mechanism for inactivation of the VHL complex during ccRCC pathogenesis. These changes not only abolished the recruitment of VHL to the CUL2–RING ubiquitin ligase complex (CRL2), resulting in HIF accumulation, but could also compromise the recruitment of Elongin A, which is an essential component of the RNA polymerase II Elongin complex[21], and of other BC-box proteins, such as SOCS3, FEM1B and LRR1, to the CRL2 complex via Elongin C (**Supplementary Fig. 11b–e**). Loss of chromosome 8 was obligatory and resulted in the total loss of wild-type *TCEB1* alleles. Nevertheless, no nonsense or truncating *TCEB1* mutations were observed, suggesting that mutated Elongin C could still retain its interactions with unknown molecules, which would be critical for tumor cell viability.

By integrating multiple layers of different comprehensive analyses, we unmasked unique correlations between somatic mutations, DNA methylation, gene expression and copy number alterations, which were also closely linked to the clinical behaviors of tumors. In particular, correlation of the cluster with hypermethylation with hyperploid status, LOH at 9p and poor prognosis was conspicuous and was in stark contrast to the correlation of the cluster with low methylation with less frequent hyperploidy or LOH at 9p and an excellent prognosis. Clinically, the discovery of the cluster of cases with hypermethylation was a notable finding, and special attention should be paid to these cases in their management and in early detection or prevention of recurrent and/or metastatic disease. Except for frequent hyperploidy and a higher *BAP1* mutation rate, the genetic basis of this cluster of cases with hypermethylation remains unclear and will require further investigation to clarify its pathophysiology.

URLs. dbSNP, http://www.ncbi.nlm.nih.gov/projects/SNP/; 1000 Genomes Project, http://www.1000genomes.org/; RepeatMasker, http://www.repeatmasker.org/; Genomonfusion (in Japanese), http://genomon.hgc.jp/rna/; CNAG/AsCNAR, http://www.genome.umin.jp/; GISTIC 2.0, http://www.broadinstitute.org/cgi-bin/cancer/publications/pub_paper.cgi?mode=view&paper_id=216&p=t; Gene Set Enrichment Analysis (GSEA), http://www.broadinstitute.org/gsea/; MSigDB,

http://www.broadinstitute.org/gsea/msigdb/index.jsp; the European Genome-phenome Archive, https://www.ebi.ac.uk/ega/.

METHODS

Methods and any associated references are available in the online version of the paper.

Accession code. Sequencing and genotype data have been deposited in the European Genome-phenome Archive (EGA) under accession EGAS00001000509.

Note: Any Supplementary Information and Source Data are available in the online version of the paper.

ACKNOWLEDGMENTS

We thank Y. Mori, M. Nakamura, N. Mizota and S. Ichimura for their technical assistance. We also thank M. Nangaku and N. Takeda for fruitful discussion and comments. We thank T. Kitamura (University of Tokyo) for providing pMXs-puro, M. Onodera (National Center for Child Health and Development, Japan) for providing pGCDNsamIRESEGFP and R.C. Mulligan (Boston Children's Hospital) for providing 293gp cells. This work was supported by KAKENHI (22134006), the Industrial Technology Research Grant Program from the New Energy and Industrial Technology Development Organization (NEDO) (08C46598a) and the Japan Society for the Promotion of Science through the Funding Program for World-Leading Innovative R&D on Science and Technology, initiated by the Council for Science and Technology Policy.

AUTHOR CONTRIBUTIONS

Y. Sato, S. Maekawa, Y.N., H.S., Y. Suzuki, S.S., K.Y. and A.K. performed DNA sequencing. Y. Shiraishi, Y.O., K.C., H.T., A.F., T.T. and S. Miyano performed bioinformatics analyses of the sequencing data. T.Y., M.S. and T.K. performed the functional analyses of Elongin C mutants. Y. Sato, A.S.-O., A.N. and M.S. performed SNP array and expression array analyses. T.S., G.N. and H.A. performed methylation analysis. H.K. and Y.H. provided specimens and were also involved in planning the project. T.M., D.M. and M.F. confirmed histological diagnosis and performed immunostaining for HIF proteins. Y. Sato, T.Y., Y.O., A.S.-O. and S.O. generated figures and tables and wrote the manuscript. S.O. led the entire project. All authors participated in the discussion and interpretation of data and results.

COMPETING FINANCIAL INTERESTS

The authors declare no competing financial interests.

1. Ferlay, J. *et al.* Estimates of worldwide burden of cancer in 2008: GLOBOCAN 2008. *Int. J. Cancer* **127**, 2893–2917 (2010).
2. Rini, B.I., Campbell, S.C. & Escudier, B. Renal cell carcinoma. *Lancet* **373**, 1119–1132 (2009).
3. Ljungberg, B. *et al.* EAU guidelines on renal cell carcinoma: the 2010 update. *Eur. Urol.* **58**, 398–406 (2010).
4. Gnarra, J.R. *et al.* Mutations of the *VHL* tumour suppressor gene in renal carcinoma. *Nat. Genet.* **7**, 85–90 (1994).
5. Gallou, C. *et al.* Mutations of the *VHL* gene in sporadic renal cell carcinoma: definition of a risk factor for VHL patients to develop an RCC. *Hum. Mutat.* **13**, 464–475 (1999).
6. Schraml, P. *et al. VHL* mutations and their correlation with tumour cell proliferation, microvessel density, and patient prognosis in clear cell renal cell carcinoma. *J. Pathol.* **196**, 186–193 (2002).
7. Herman, J.G. *et al.* Silencing of the *VHL* tumor-suppressor gene by DNA methylation in renal carcinoma. *Proc. Natl. Acad. Sci. USA* **91**, 9700–9704 (1994).
8. Varela, I. *et al.* Exome sequencing identifies frequent mutation of the SWI/SNF complex gene *PBRM1* in renal carcinoma. *Nature* **469**, 539–542 (2011).
9. Dalgliesh, G.L. *et al.* Systematic sequencing of renal carcinoma reveals inactivation of histone modifying genes. *Nature* **463**, 360–363 (2010).
10. Peña-Llopis, S. *et al.* BAP1 loss defines a new class of renal cell carcinoma. *Nat. Genet.* **44**, 751–759 (2012).
11. Guo, G. *et al.* Frequent mutations of genes encoding ubiquitin-mediated proteolysis pathway components in clear cell renal cell carcinoma. *Nat. Genet.* **44**, 17–19 (2012).
12. Greenman, C. *et al.* Patterns of somatic mutation in human cancer genomes. *Nature* **446**, 153–158 (2007).
13. Guichard, C. *et al.* Integrated analysis of somatic mutations and focal copy-number changes identifies key genes and pathways in hepatocellular carcinoma. *Nat. Genet.* **44**, 694–698 (2012).
14. Huang, J. *et al.* Exome sequencing of hepatitis B virus–associated hepatocellular carcinoma. *Nat. Genet.* **44**, 1117–1121 (2012).
15. Sung, W.K. *et al.* Genome-wide survey of recurrent HBV integration in hepatocellular carcinoma. *Nat. Genet.* **44**, 765–769 (2012).
16. Fujimoto, A. *et al.* Whole-genome sequencing of liver cancers identifies etiological influences on mutation patterns and recurrent mutations in chromatin regulators. *Nat. Genet.* **44**, 760–764 (2012).
17. Gerlinger, M. *et al.* Intratumor heterogeneity and branched evolution revealed by multiregion sequencing. *N. Engl. J. Med.* **366**, 883–892 (2012).
18 Hakimi, A.A. *et al.* Adverse outcomes in clear cell renal cell carcinoma with mutations of 3p21 epigenetic regulators *BAP1* and *SETD2*: a report by MSKCC and the KIRC TCGA Research Network. *Clin. Cancer Res.* **19**, 3259–3267 (2013).
19. Hakimi, A.A. *et al.* Clinical and pathologic impact of select chromatin-modulating tumor suppressors in clear cell renal cell carcinoma. *Eur. Urol.* **63**, 848–854 (2013).
20. Kapur, P. *et al.* Effects on survival of *BAP1* and *PBRM1* mutations in sporadic clear-cell renal-cell carcinoma: a retrospective analysis with independent validation. *Lancet Oncol.* **14**, 159–167 (2013).
21. Aso, T., Lane, W.S., Conaway, J.W. & Conaway, R.C. Elongin (SIII): a multisubunit regulator of elongation by RNA polymerase II. *Science* **269**, 1439–1443 (1995).
22. Kamura, T. *et al.* Activation of HIF1a ubiquitination by a reconstituted von Hippel-Lindau (VHL) tumor suppressor complex. *Proc. Natl. Acad. Sci. USA* **97**, 10430–10435 (2000).
23. Stebbins, C.E., Kaelin, W.G. Jr. & Pavletich, N.P. Structure of the VHL-ElonginC-ElonginB complex: implications for VHL tumor suppressor function. *Science* **284**, 455–461 (1999).
24. Takagi, Y., Pause, A., Conaway, R.C. & Conaway, J.W. Identification of elongin C sequences required for interaction with the von Hippel-Lindau tumor suppressor protein. *J. Biol. Chem.* **272**, 27444–27449 (1997).
25. Delhommeau, F. *et al.* Mutation in *TET2* in myeloid cancers. *N. Engl. J. Med.* **360**, 2289–2301 (2009).
26. Langemeijer, S.M. *et al.* Acquired mutations in *TET2* are common in myelodysplastic syndromes. *Nat. Genet.* **41**, 838–842 (2009).
27. Chen, Q., Chen, Y., Bian, C., Fujiki, R. & Yu, X. TET2 promotes histone O-GlcNAcylation during gene transcription. *Nature* **493**, 561–564 (2013).
28. The Cancer Genome Atlas Network. Comprehensive molecular characterization of human colon and rectal cancer. *Nature* **487**, 330–337 (2012).
29. Zimmerman, E.S., Schulman, B.A. & Zheng, N. Structural assembly of cullin–RING ubiquitin ligase complexes. *Curr. Opin. Struct. Biol.* **20**, 714–721 (2010).
30. Padmanabhan, B. *et al.* Structural basis for defects of Keap1 activity provoked by its point mutations in lung cancer. *Mol. Cell* **21**, 689–700 (2006).
31. Shibata, T. *et al.* Cancer related mutations in *NRF2* impair its recognition by Keap1-Cul3 E3 ligase and promote malignancy. *Proc. Natl. Acad. Sci. USA* **105**, 13568–13573 (2008).
32. Kim, Y.R. *et al.* Oncogenic *NRF2* mutations in squamous cell carcinomas of oesophagus and skin. *J. Pathol.* **220**, 446–451 (2010).
33. Adam, J. *et al.* Renal cyst formation in Fh1-deficient mice is independent of the Hif/Phd pathway: roles for fumarate in KEAP1 succination and Nrf2 signaling. *Cancer Cell* **20**, 524–537 (2011).
34. Kinch, L., Grishin, N.V. & Brugarolas, J. Succination of Keap1 and activation of Nrf2-dependent antioxidant pathways in FH-deficient papillary renal cell carcinoma type 2. *Cancer Cell* **20**, 418–420 (2011).
35. Ooi, A. *et al. CUL3* and *NRF2* mutations confer an NRF2 activation phenotype in a sporadic form of papillary renal cell carcinoma. *Cancer Res.* **73**, 2044–2051 (2013).
36. Kucejova, B. *et al.* Interplay between pVHL and mTORC1 pathways in clear-cell renal cell carcinoma. *Mol. Cancer Res.* **9**, 1255–1265 (2011).
37. Yoshida, K. *et al.* Frequent pathway mutations of splicing machinery in myelodysplasia. *Nature* **478**, 64–69 (2011).
38. Kadoch, C. *et al.* Proteomic and bioinformatic analysis of mammalian SWI/SNF complexes identifies extensive roles in human malignancy. *Nat. Genet.* **45**, 592–601 (2013).
39. Clark, J. *et al.* Fusion of splicing factor genes *PSF* and *NonO* (*p54^{nrb}*) to the *TFE3* gene in papillary renal cell carcinoma. *Oncogene* **15**, 2233–2239 (1997).
40. Ross, H. & Argani, P. Xp11 translocation renal cell carcinoma. *Pathology* **42**, 369–373 (2010).
41. Kuroda, N. *et al.* Review of renal carcinoma associated with Xp11.2 translocations/*TFE3* gene fusions with focus on pathobiological aspect. *Histol. Histopathol.* **27**, 133–140 (2012).
42. Brannon, A.R. *et al.* Molecular stratification of clear cell renal cell carcinoma by consensus clustering reveals distinct subtypes and survival patterns. *Genes Cancer* **1**, 152–163 (2010).
43. Huang, W., Sherman, B.T. & Lempicki, R.A. Systematic and integrative analysis of large gene lists using DAVID bioinformatics resources. *Nat. Protoc.* **4**, 44–57 (2009).

ONLINE METHODS

Subjects and materials. Paired tumor-normal DNA was isolated from 240 ccRCC specimens and subjected to comprehensive molecular analyses after written informed consent was obtained. Matched normal specimens for germline controls were obtained from adjacent normal kidney tissue or from peripheral blood specimens (**Supplementary Note**). No subjects received preoperative treatments, including immunotherapies or molecular targeted therapies. Histopathological specimens were reviewed to confirm that the tumor specimens were histologically consistent with ccRCC (**Supplementary Figs. 14** and **22**). This study was approved by the ethics committee of the Graduate School of Medicine at the University of Tokyo.

Whole-genome sequencing. For whole-genome sequencing, genomic DNA was sonicated to generate approximately 400-bp fragments and was analyzed by HiSeq 2000 with the 100-bp paired-end read option according to the manufacturer's protocol.

FASTQ sequences generated by CASAVA 1.8 were aligned to the human reference genome (hg19) using Burrows-Wheeler Aligner (BWA)[44] version 0.5.8. We attempted to realign unmapped or poorly mapped reads using BLAT[45]. For both SNVs and indels, the variant bases found in ≥7 reads in tumor samples and in ≤1 (SNVs) or 0 (indels) reads in germline samples were designated as variants. Within noncoding regions, variants found on average in 1% of the total reads in 13 unrelated germline samples were excluded from further analysis owing to the high probability that they represented false positives. Synonymous variants and variants found in either an in-house SNP database constructed from exome sequence data from 98 germline samples, dbSNP131 or the 1000 Genomes Project database were excluded. We also excluded SNVs that were in a tandem repeat region identified using tandem repeats finder[46] and indels that were in RepeatMasker.

To detect structural variations, soft-clipped sequences that could be mapped to unique genomic positions were collected. Structural variation candidates were called if they had >4 supporting read pairs in total and at least 1 read pair from each shore of the breakpoint. Structural variations having a contig sequence that could be aligned to an alternate assembly of the hg19 genome with >93% identity were excluded as false positives. Structural variations with a read depth of >150 at either breakpoint were considered to be in a repeat element and were excluded.

Whole-exome and RNA sequencing. Whole-exome sequencing was performed using target capture with SureSelect v.4 followed by sequencing as previously described[37]. Mutation calling used the EBcall algorithm[47]. For targeted sequencing, 3 mg of whole-genome DNA was amplified using the REPLI-g kit (Qiagen) and sonicated to generate a peak target size of 200 bp. Captured targets were sequenced using the Illumina HiSeq2000 platform with the 100-bp paired-end read option. A custom bait (SureSelect) library for a panel of eight genes was used for target capture, and high-throughput sequencing was performed using the 100-bp paired-end read option. Libraries for RNA sequencing were generated using the TruSeq RNA Sample Preparation kit (Illumina) and were analyzed using the Illumina HiSeq 2000 platform with 100-bp paired-end reads according to the manufacturer's protocol. Gene fusion detection was performed using Genomon-fusion.

To detect significantly mutated genes, the background mutation rate was calculated for each gene on the basis of data from the current whole-exome sequencing study, taking into consideration the effect of the replication timing of the gene during DNA replication on the background mutation rate as previously described[48,49]. Mutations showing significantly higher mutation frequencies compared to the corresponding background mutation rate were adopted as significantly mutated genes, with Benjamini-Hochberg correction applied.

Analysis of significantly mutated pathways. To detect significantly mutated pathways, each pathway registered in the Kyoto Encyclopedia of Genes and Genomes (KEGG), BioCarta, Reactome, Sigma-Aldrich and Signaling Transduction KE was tested with the PathScan package[50] on the basis of the background mutation rate observed in whole-exome sequencing data. We excluded somatic mutations that were not observed in RNA sequencing because we expected that they would make only a small contribution to pathogenesis. Benjamini-Hochberg correction was applied.

PCR-based deep sequencing. To validate somatic mutations and estimate mutant allele frequencies, we conducted deep sequencing using the Illumina MiSeq platform. We randomly selected SNVs and indels called through our pipeline, finding that TPRs were 99% (476/477) for coding SNVs, 99% (93/94) for noncoding SNVs, 96% (29/30) for coding indels and 97% (32/33) for noncoding indels in whole-genome sequencing. In whole-exome sequencing, TPRs were 96% (504/525) for SNVs and 96% (55/57) for indels. Primer sequences are shown in **Supplementary Tables 13** and **14**.

Microarray analyses. Global DNA methylation profiles were analyzed using the Infinium HumanMethylation450 BeadChip (Illumina) according to the manufacturer's instructions. To determine DNA methylation profiles, the following filtering steps were adopted to select probes for unsupervised clustering analysis. We first removed probes that were designed for sequences on the X and Y chromosomes. Second, we selected probes with variance ranked in the top 1% of the remaining probes. We then performed unsupervised hierarchical clustering with 3,562 probes, identifying 3 distinct clusters. The β values of 1,672 probes, containing 1,228 genes, that were differentially methylated in the high and low-intermediate groups were represented graphically using a heatmap. Genome-wide analysis of DNA copy number was conducted for 240 tumor-normal specimens using the Affymetrix GeneChip Human Mapping 250K NspI Array according to the manufacturer's protocol. Microarray data were analyzed to determine total and allele-specific copy numbers using CNAG/AsCNAR[51,52]. Significant focal copy number alterations were identified using GISTIC 2.0. Gene expression analysis used 500 ng of total RNA extracted from each tumor ($n = 101$) using the Human Gene Expression 4x44K v2 Microarray (Agilent) according to the manufacturer's instructions. GSEA was performed for both gene expression and DNA methylation using the curated gene sets (c2) acquired from MSigDB.

Multivariate analysis. To evaluate the impact of the mutation status of *PBRM1*, *BAP1* and *SETD2* on overall survival and disease-free survival, we performed multivariate analysis of the three genes for an extended cohort of 240 ccRCC cases.

Immunostaining for HIF-1α, HIF-2α and TFE3. Immunohistochemistry used mouse monoclonal antibody against HIF-1α (1:300 dilution; clone H1alpha67, NB100-105, Novus Biomedicals) and rabbit polyclonal antibody against HIF-2α (1:1,000 dilution; NB100-122, Novus Biomedicals). Cases were considered positive for expression when >5% of tumor cells showed nuclear immunoreactivity. Expression-positive cases were further classified on the basis of the intensity of nuclear immunoreactivity: 1+, mild; 2+, moderate; 3+, strong. Immunohistochemistry for TFE3 was performed as previously described[53] (sc-5958, Santa Cruz Biotechnology).

doi:10.1038/ng.2699

Plasmid construction. Full-length *TCEB1* cDNA was obtained by PCR amplification of DNA extracted in normal human colon and was cloned adjacent to a sequence encoding three copies of a hemagglutinin (HA) tag at the N terminus of the protein. This construct was subcloned into pMXs-puro[54], pGCDNsamIRESEGFP[55] and pCI-neo (Promega). cDNA encoding the Tyr79Cys and Ala100Pro mutants was obtained from *in vitro* mutagenesis using wild-type *TCEB1* cDNA as the template and the QuikChange Site-Directed Mutagenesis kit (Stratagene). In the pGCDNsamIRESEGFP-*TCEB1* constructs, four synonymous nucleotide substitutions, c.210A>C (p.Leu70Leu) and c.211_213TCG>AGC (p.Ser71Ser), were introduced to protect the transcripts from targeting by siRNA designed for endogenous *TCEB1* transcripts using PrimeSTAR HS DNA Polymerase (Takara Bio) according to the manufacturer's protocol. Human *TCEB2* cDNA was obtained with the same method as for *TCEB1* and was cloned into pCI-neo. For *VHL*, *FEM1B*, *TCEB3*, *LRR1* and *SOCS3*, each cDNA was tagged with three copies of sequence encoding a Flag epitope (Flag tag) at its N terminus and was cloned into pcDNA3/Puro[56].

Cell culture and gene transfer. HeLa, HEK 293T and 293gp cells were maintained in DMEM (Gibco) supplemented with 10% FCS and 1% penicillin and streptomycin in a humidified atmosphere with 5% CO_2 or 10% CO_2 at 37 °C. HeLa cells were engineered to stably express wild-type or mutant *TCEB1* or indicated empty vectors (mock) using retrovirus-mediated gene transfer (pMXs-puro-*TCEB1* or pGCDNsamIRESEGFP-*TCEB1*)[37]. HeLa cells transfected with pMXs-puro were subjected to puromycin selection. Cells transduced with pGCDNsamIRESEGFP were sorted for green fluorescent protein (GFP) signal using a flow cytometer (BD FACSAria III, Becton Dickinson). HEK 293T cells were transiently cotransfected with the indicated genes by the calcium phosphate transfection method. Cells were used for experiments after 48 h in culture.

RNA interference. Synthetic siRNAs were obtained from Takara Bio (**Supplementary Table 7b**). HeLa cells were transfected with each siRNA using Lipofectamine 2000 (Invitrogen) according to the manufacturer's instructions. Cells were used for experiments after incubation for 48 h.

Quantitative RT PCR. RNA (500 ng) extracted from the indicated cells using the RNA RNeasy Mini kit (Qiagen) was subjected to reverse transcription using the ReverTra Ace qPCR RT kit (Toyobo) according to the manufacturer's protocol. Quantitative expression levels of mRNA were measured as described previously[37]. Primers used for quantitative RT-PCR are listed in **Supplementary Table 7c**.

Antibodies. Antibodies used for immunoblot analysis are described in **Supplementary Table 15**. Antibodies were from commercial companies except for antibody against Elongin B[57].

Protein extraction and immunoblot analysis. Cells were lysed in RIPA buffer (Santa Cruz Biotechnology). Lysates were subjected to SDS-PAGE. Proteins were separated and electrophoretically transferred to polyvinylidene difluoride (PVDF) membranes. Membranes were incubated with the indicated antibodies, and proteins were detected using Immobilon Western Chemiluminescent HRP Substrate (Millipore).

Immunoprecipitation. Cells transfected with the indicated vectors were lysed. For endogenous VHL stabilization, HeLa cells transfected with pMXs-puro-*TCEB1* were treated with 10 mM MG132 for 6 h before harvesting. HEK 293T cells cotransfected with constructs encoding HA-TCEB1, untagged TCEB2 and Flag-tagged binding proteins were subjected to immunoprecipitation using an antibody to HA or Flag, and immunoblotting was performed as described.

44. Li, H. & Durbin, R. Fast and accurate short read alignment with Burrows-Wheeler transform. *Bioinformatics* **25**, 1754–1760 (2009).
45. Kent, W.J. BLAT—the BLAST-like alignment tool. *Genome Res.* **12**, 656–664 (2002).
46. Benson, G. Tandem repeats finder: a program to analyze DNA sequences. *Nucleic Acids Res.* **27**, 573–580 (1999).
47. Shiraishi, Y. *et al.* An empirical Bayesian framework for somatic mutation detection from cancer genome sequencing data. *Nucleic Acids Res.* **41**, e89 (2013).
48. Hellmann, I. *et al.* Why do human diversity levels vary at a megabase scale? *Genome Res.* **15**, 1222–1231 (2005).
49. Stamatoyannopoulos, J.A. *et al.* Human mutation rate associated with DNA replication timing. *Nat. Genet.* **41**, 393–395 (2009).
50. Wendl, M.C. *et al.* PathScan: a tool for discerning mutational significance in groups of putative cancer genes. *Bioinformatics* **27**, 1595–1602 (2011).
51. Nannya, Y. *et al.* A robust algorithm for copy number detection using high-density oligonucleotide single nucleotide polymorphism genotyping arrays. *Cancer Res.* **65**, 6071–6079 (2005).
52. Yamamoto, G. *et al.* Highly sensitive method for genomewide detection of allelic composition in nonpaired, primary tumor specimens by use of Affymetrix single-nucleotide-polymorphism genotyping microarrays. *Am. J. Hum. Genet.* **81**, 114–126 (2007).
53. Tsuji, K., Ishikawa, Y. & Imamura, T. Technique for differentiating alveolar soft part sarcoma from other tumors in paraffin-embedded tissue: comparison of immunohistochemistry for TFE3 and CD147 and of reverse transcription polymerase chain reaction for *ASPSCR1-TFE3* fusion transcript. *Hum. Pathol.* **43**, 356–363 (2012).
54. Morita, S., Kojima, T. & Kitamura, T. Plat-E: an efficient and stable system for transient packaging of retroviruses. *Gene Ther.* **7**, 1063–1066 (2000).
55. Nabekura, T., Otsu, M., Nagasawa, T., Nakauchi, H. & Onodera, M. Potent vaccine therapy with dendritic cells genetically modified by the gene-silencing-resistant retroviral vector GCDNsap. *Mol. Ther.* **13**, 301–309 (2006).
56. Kamura, T. *et al.* VHL-box and SOCS-box domains determine binding specificity for Cul2-Rbx1 and Cul5-Rbx2 modules of ubiquitin ligases. *Genes Dev.* **18**, 3055–3065 (2004).
57. Garrett, K.P. *et al.* Positive regulation of general transcription factor SIII by a tailed ubiquitin homolog. *Proc. Natl. Acad. Sci. USA* **92**, 7172–7176 (1995).

Circulation
JOURNAL OF THE AMERICAN HEART ASSOCIATION

American Heart Association®

Enhanced Survival of Transplanted Human Induced Pluripotent Stem Cell–Derived Cardiomyocytes by the Combination of Cell Sheets With the Pedicled Omental Flap Technique in a Porcine Heart

Masashi Kawamura, Shigeru Miyagawa, Satsuki Fukushima, Atsuhiro Saito, Kenji Miki, Emiko Ito, Nagako Sougawa, Takuji Kawamura, Takashi Daimon, Tatsuya Shimizu, Teruo Okano, Koichi Toda and Yoshiki Sawa

Circulation. 2013;128:S87-S94
doi: 10.1161/CIRCULATIONAHA.112.000366
Circulation is published by the American Heart Association, 7272 Greenville Avenue, Dallas, TX 75231

Print ISSN: 0009-7322. Online ISSN: 1524-4539

Enhanced Survival of Transplanted Human Induced Pluripotent Stem Cell–Derived Cardiomyocytes by the Combination of Cell Sheets With the Pedicled Omental Flap Technique in a Porcine Heart

Masashi Kawamura, MD; Shigeru Miyagawa, MD, PhD; Satsuki Fukushima, MD, PhD; Atsuhiro Saito, PhD; Kenji Miki, PhD; Emiko Ito, PhD; Nagako Sougawa, PhD; Takuji Kawamura, MD; Takashi Daimon, PhD; Tatsuya Shimizu, MD, PhD; Teruo Okano, PhD; Koichi Toda, MD, PhD; Yoshiki Sawa, MD, PhD

Background—Transplantation of cardiomyocytes that are derived from human induced pluripotent stem cell–derived cardiomyocytes (hiPS-CMs) shows promise in generating new functional myocardium in situ, whereas the survival and functionality of the transplanted cells are critical in considering this therapeutic impact. Cell-sheet method has been used to transplant many functional cells; however, potential ischemia might limit cell survival. The omentum, which is known to have rich vasculature, is expected to be a source of blood supply. We hypothesized that transplantation of hiPS-CM cell sheets combined with an omentum flap may deliver a large number of functional hiPS-CMs with enhanced blood supply.

Methods and Results—Retrovirally established human iPS cells were treated with Wnt signaling molecules to induce cardiomyogenic differentiation, followed by superparamagnetic iron oxide labeling. Cell sheets were created from the magnetically labeled hiPS-CMs using temperature-responsive dishes and transplanted to porcine hearts with or without the omentum flap (n=8 each). Two months after transplantation, the survival of superparamagnetic iron oxide–labeled hiPS-CMs, assessed by MRI, was significantly greater in mini-pigs with the omentum than in those without it; histologically, vascular density in the transplanted area was significantly greater in mini-pigs with the omentum than in those without it. The transplanted tissues contained abundant cardiac troponin T–positive cells surrounded by vascular-rich structures.

Conclusions—The omentum flap enhanced the survival of hiPS-CMs after transplantation via increased angiogenesis, suggesting that this strategy is useful in clinical settings. The combination of hiPS-CMs and the omentum flap may be a promising technique for the development of tissue-engineered vascular-rich new myocardium in vivo. **(*Circulation*. 2013;128[suppl 1]:S87-S94.)**

Key Words: cell transplantation ■ induced pluripotent stem cells ■ regeneration

Stem cell therapy shows promise in the treatment of heart failure. However, the therapeutic benefits proven by clinical studies in the past decade were only modest, indicating that further investigations and refinements are required to establish this treatment in the clinical arena.[1,2] The success of cell transplantation therapy for heart failure is dependent on the choice of cell source, cell delivery method, and target cardiac pathology. In these previous clinical trials, transplantation of somatic tissue–derived stem or progenitor cells has shown no or low cardiomyogenic differentiation capacity in vivo, but contributed to functional recovery via paracrine effects, potentially limiting the therapeutic effects, in particular, in treating severe heart failure.[1–4] In addition, it has been shown that direct intramyocardial or intracoronary injection of dissociated single cells, which was used in most of the clinical studies, yields <10% of engraftment rate of the cells immediately after transplantation, indicating that further refinement of the cell delivery method would be required to increase cell engraftment and enhance the consequent therapeutic effects.[1,2]

Human induced pluripotent stem (hiPS) cells are initially established by nuclear reprogramming of somatic cells.[5,6] hiPS cell carries a capacity of unlimited proliferation and differentiation to cardiomyocyte.[7] Transplantation of hiPS-derived cardiomyocytes (hiPS-CMs) would have, thus, a potential to

From the Department of Cardiovascular Surgery, Osaka University Graduate School of Medicine, Suita, Osaka, Japan (M.K., S.M., S.F., K.M., E.I., N.S., T.K., K.T., Y.S.); Medical Center for Translational Research, Osaka University Hospital, Suita, Osaka, Japan (A.S.); Department of Biostatistics, Hyogo College of Medicine, Nishinomiya, Hyogo, Japan (T.D.); Institute of Advanced Biomedical Engineering and Science, Tokyo Women's Medical University, Tokyo, Japan (T.S., T.O.).

Presented at the 2012 American Heart Association meeting in Los Angeles, CA, November 3–7, 2012.

The online-only Data Supplement is available with this article at http://circ.ahajournals.org/lookup/suppl/doi:10.1161/CIRCULATIONAHA.112.000366/-/DC1.

Correspondence to Yoshiki Sawa, MD, PhD, Department of Cardiovascular Surgery, Osaka University Graduate School of Medicine, 2-2(E1) Yamadaoka, Suita, Osaka 565-0871, Japan. E-mail sawa-p@surg1.med.osaka-u.ac.jp

Circulation **is available at http://circ.ahajournals.org** **DOI: 10.1161/CIRCULATIONAHA.112.000366**

increase the functional cardiomyocytes in damaged heart tissue to mechanically contribute to cardiac function. In addition, the recently developed scaffoldless tissue engineering technique of cell-sheet engineering is applicable to myocardial regeneration therapy.[8] This technique preserves extracellular matrix without artificial scaffolds, which may prevent cell detachment–associated anoikis.[9] In contrast to the needle injection technique, the cell-sheet technique can deliver a large number of cells to the damaged myocardium without loss of transplanted cells or injury to the host myocardium.[10,11] Importantly, this method has already shown feasibility and safety in the clinical study.[12] On these bases, we studied the therapeutic efficacy of transplantation of hiPS-CMs with the cell-sheet method in a porcine chronic ischemic cardiomyopathy model.[13] This study, however, showed that the transplanted cells rarely survived in the heart long-term, possibly because of poor vascular network support from the native tissue.

The omentum has been historically used in surgical revascularization for patients with ischemic heart disease[14–16] and is also known to have rich vasculature and angiogenic factors.[17,18] Importantly, we reported that a pedicle omentum flap covering the transplanted skeletal myoblast cell sheets enhanced angiogenesis over the cell-sheet–transplanted territory, survival of cells, and therapeutic effects.[19] We herein hypothesized that covering with an omentum flap may enhance the survival of transplanted hiPS-CM cell sheets via the promotion of angiogenesis over the transplanted territory. In this study, we compared the survival of hiPS-CMs, with or without a pedicle omentum flap, after transplantation to the mini-pig heart, and we examined whether the omentum enhanced the angiogenic capacity of hiPS-CM sheets in vivo.

Materials and Methods

All experimental procedures were approved by the institutional ethics committee. Animal care was conducted humanely in compliance with the Principles of Laboratory Animal Care formulated by the National Society for Medical Research and the Guide for the Care and Use of Laboratory Animals prepared by the Institute of Animal Resources and published by the National Institutes of Health (publication no. 85-23, revised 1996).

Preparation of SPIO-Labeled hiPS-CM Cell Sheets

The hiPS cell line 201B7 that was generated using the 4 transcription factors Oct4, Sox2, Klf4, and c-Myc was used in this study.[5] Culture of the hiPS cells, formation of the embryoid bodies, and subsequent cardiomyogenic differentiation and purification were performed as described previously to generate hiPS-CMs.[13] The purified hiPS-CMs were then labeled with the superparamagnetic iron oxide (SPIO) ferucarbotran (Resovist; Bayer Pharma, Berlin, Germany) using the hemagglutinating virus of Japan envelope vector (GenomOne-Neo; Ishihara Sangyo, Osaka, Japan).[20,21] Subsequently, human mesenchymal stem cells (Lonza, Basel, Switzerland) were seeded at a density of 5×10^6 cells/dish onto 10-cm UpCell dishes, on which the SPIO-labeled hiPS-CMs were grown. The next day, the dishes were incubated at room temperature, which induced the cells to detach spontaneously to form scaffold-free hiPS-CM cell sheets.

Flow Cytometry

Dissociated cells after hiPS cell differentiation were fixed, permeabilized, and labeled with anticardiac isoform of troponin T (cTNT; clone 13211; Thermo Fisher scientific, Runcorn, UK) conjugated with Alexa-488 using Zenon technology (Invitrogen), followed by analysis on BD FACSCanto II (BD Biosciences) with BD FACSDiva Software (BD Biosciences).

Study Protocol

Normal 16 female mini-pigs (Japan Farm Co Ltd, Kagoshima, Japan) weighing 20 to 25 kg were randomly divided into 2 groups (n=8 each) to perform hiPS-CM cell-sheet transplantation either with or without the pedicle omentum translocation. All animals were immunosuppressed by daily administration of tacrolimus (0.75 mg/kg; Astellas, Tokyo, Japan), mycophenolate mofetil (500 mg; Teva Czech Industries s.r.o, Opava, Czech), and prednisolone (20 mg; Takeda Pharmaceutical Co Ltd, Osaka, Japan) daily from 5 days before transplantation until euthanasia. Cardiac MRI scans were taken on the same mini-pigs at 1 week, 4 weeks, and 8 weeks after transplantation. After the final scan, the mini-pigs were humanely euthanized for analysis (Figure 1A).

Transplantation of SPIO-Labeled hiPS-CM Cell Sheets Covered With the Pedicle Omentum

All animals were preanesthetized with ketamine hydrochloride (20 mg/kg; Daiichi Sankyo, Tokyo, Japan) and xylazine (2 mg/kg; Bayer HealthCare, Leverkusen, Germany), intubated endotracheally, and maintained by continuous infusion of propofol (6 mg/kg per hour; AstraZeneca K.K., Osaka, Japan) and vecuronium bromide (0.05 mg/kg per hour; Daiichi Sankyo). Seven SPIO-labeled hiPS-CM sheets were placed on the epicardium via the median sternotomy. In the case of transplantation of the cell sheet covered with the pedicled omentum, the omentum was mobilized to the mediastinal space via additional small upper midline laparotomy, preserving both gastroepiploic arteries and their arcade. Initially, 4 hiPS-CM cell sheets were placed on the epicardium and covered with the omentum. The remaining 3 hiPS-CM cell sheets, then, were placed on the covering omentum and covered with the omentum again (Figure 1B). The omentum was stitched and fixed on the excised pericardium (Figure 1C). Mini-pigs were then allowed to recover and were later humanely euthanized.

Cardiac MRI

ECG-gated cardiac MRI (CMR) was performed under general anesthesia with an 8-channel cardiac coil wrapped around the chest wall.[22] CMR images were acquired on a 1.5-T MR scanner (Signa EXCITE XI TwinSpeed; GE Medical Systems, Milwaukee, WI). To assess SPIO-labeled hiPS-CM detection, animals were imaged 1 week after transplantation. In addition, 1 animal was reimaged at 4 and 8 weeks after transplantation to detect SPIO-labeled hiPS-CM retention. Short-axis images with 8-mm slice thickness, including the entire heart, were obtained by pulse parameters for cardiac-gated, fast gradient–recalled echo. The SPIO-labeled hiPS-CM hypointense area was measured using planimetry of fast gradient–recalled echo images on a workstation (Virtual Place Lexus64; AZE, Tokyo, Japan). The survival proportion of hiPS-CMs was determined using the hypointense area at 4 and 8 weeks after transplantation divided by the area at 1 week after transplantation as the baseline.

Histology and Immunohistolabeling

The hiPS-CM cell sheets and the excised heart specimens were either embedded in paraffin or optimal cutting temperature compound (Tissueb Tek; Sakura Finetek, Torrance, CA) for frozen section. The paraffin-embedded sections were stained with hematoxylin–eosin or Prussian blue that visualizes iron contents. Ten different fields were randomly selected. The number of spindle-shaped cells with a nucleus and iron in the cytoplasm in each field was counted with a light microscopy under high-power magnification (×400). Cells from 10 fields were averaged, and the results are expressed as cell density (per high-power field). In addition, the paraffin-embedded sections were immunolabeled with anti-human von Willebrand factor antibody (Dako, Glostrup, Denmark) and visualized with the horseradish peroxidase-based EnVision kit (Dako). Ten different fields were randomly selected, and the number of von Willebrand factor–positive

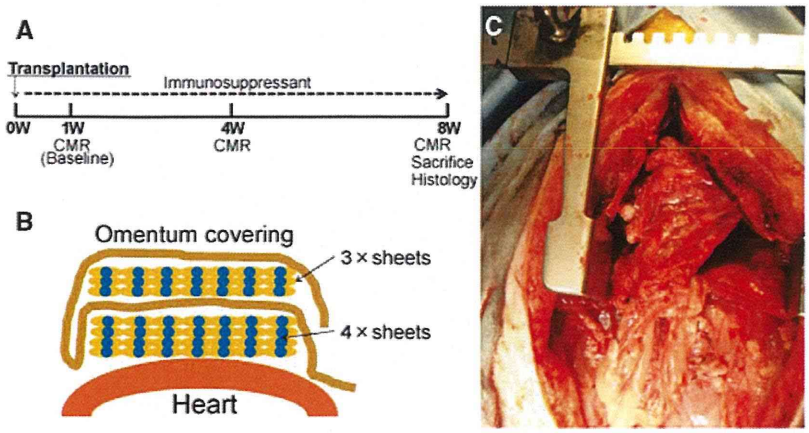

Figure 1. Study protocol of the mini-pig experiment and operative procedure. **A**, Schedule of cardiac MRI (CMR) and histological evaluations. **B**, Procedural scheme of cell-sheet transplantation with the omentum. **C**, Image taken after treatment. The omentum is mobilized and transplanted with the cell sheets on the heart through median sternotomy with an additional upper midline laparotomy.

cells in each field was counted using a light microscope under high-power magnification (×200). The stained blood vessels from the 10 fields were averaged and the results expressed as vascular density (per square millimeter). The frozen sections were immunolabeled with anti-cTNT antibody (1:100 dilution; Abcam, Cambridge, UK) and anti-CD68 antibody for macrophages (1:100 dilution, Abcam) as primary antibodies and visualized with AlexaFluor488–conjugated goat anti-mouse (Invitrogen) and AlexaFluor555–conjugated goat anti-rabbit (Invitrogen) as secondary antibodies. Nuclei were counterstained with 4′,6-diamidino-2-phenylindole (Dojindo, Tokyo, Japan) and assessed using the Biorevo BZ-9000 (Keyence) or confocal microscopy (Olympus Japan, FV1000-D IX81, Tokyo, Japan). SPIO particles of Prussian blue staining were visualized by differential interference contrast of confocal microscopy.

Real-Time Polymerase Chain Reaction

Total RNA was extracted from cardiac tissue and reverse transcribed using Omniscript reverse transcriptase (Qiagen, Hilden, Germany) with random primers (Invitrogen), and the resulting cDNA was used for real-time polymerase chain reaction with the ABI PRISM 7700 (Applied Biosystems, Stockholm, Sweden) system using pig-specific primers (Applied Biosystems) for vascular endothelial growth factor (VEGF), basic fibroblast growth factor, and stromal-derived factor-1 (SDF-1). Each sample was analyzed in triplicate for each gene studied. Data were normalized to GAPDH expression level. For relative expression analysis, the delta-delta Ct method was used, and values of the cell-sheet transplantation without the omentum were used as reference values.

Statistical Analysis

Data are expressed as means±SDs. Comparisons between 2 groups were made using Welch *t* test. Cell survival proportion over time was assessed by repeated-measures ANOVA with group, time, and group×time interaction effects. All *P* values are 2-sided, and values of $P<0.05$ were considered to indicate statistical significance. Statistical analyses were performed using JMP 9.02 (SAS Institute, Cary, NC).

Results

Generation of SPIO-Labeled hiPS-CM Cell Sheets

Cardiomyogenic differentiation of hiPS cells was induced by treatment of the embryoid bodies formed from cultured hiPS cells with Wnt3a and R-spondin-1. Subsequently, the differentiated hiPS cells were purified by culture in glucose-free medium to yield ≈1 to 2×10^7 hiPS-CMs. Approximately 80% (83.6±8.1%) of the hiPS-CMs were positive for cTNT, as determined by flow cytometry (Figure 2A). After SPIO labeling to the hiPS-CMs, human mesenchymal stem cells were added to the hiPS-CM culture. Subsequently, culture in the thermo-responsive dishes yielded round-shaped hiPS-CM cell sheets (Figure 2B). The hiPS-CMs on the sheet continued to beat before and after detaching from culture surface (Movies I and II in the online-only Data Supplement). Immunohistolabeling showed that the large number of cells in the hiPS-CM cell sheets were homogeneously positive for cTNT (Figure 2C). Prussian blue staining confirmed that the hiPS-CMs contained iron in the cytoplasm (Figure 2D).

In Vivo Analysis of Survival of Transplanted SPIO-Labeled hiPS-CMs by Serial CMR

Transplantation of the same number of hiPS-CM cell sheets with or without the omentum covering was successfully performed via median sternotomy in 16 normal mini-pigs. There was no mortality related to the procedure or otherwise before the planned euthanasia. In addition, the omentum was attached to the surface of the heart in all mini-pigs with the omentum. CMRs were performed to assess the survival of transplanted SPIO-labeled hiPS-CMs at 1 week (baseline), 4 weeks, and 8 weeks after cell transplantation.

SPIO signals were clearly identified as the hypointense area in the surface of the left ventricle by CMR in all mini-pigs throughout the study period (Figure 3A). SPIO-positive hypointense area was gradually decreased in both the groups during the 8 weeks, whereas the SPIO-positive area was larger and thicker in mini-pigs with the omentum compared with those without the omentum during the study period. The survival proportion of the SPIO-labeled hiPS-CMs was determined by the formula that the hypointense area at 4 and 8 weeks after transplantation was divided by the area at 1 week after transplantation as baseline. Both groups showed steady decrease in the cell survival during the 7 weeks, whereas the proportion of decrease was significantly less in mini-pigs with the omentum than in those without it at 4 weeks (92±10% versus 60±10%) and 8 weeks (78±10% versus 42±9%) after treatment ($P<0.0001$ for interaction effect of time and group in the repeated ANOVA; Figure 3B).

Histological Evaluation of Transplanted hiPS-CMs With or Without the Omentum

Excised heart tissues at 8 weeks after transplantation were assessed by histology. The transplanted hiPS-CMs and the

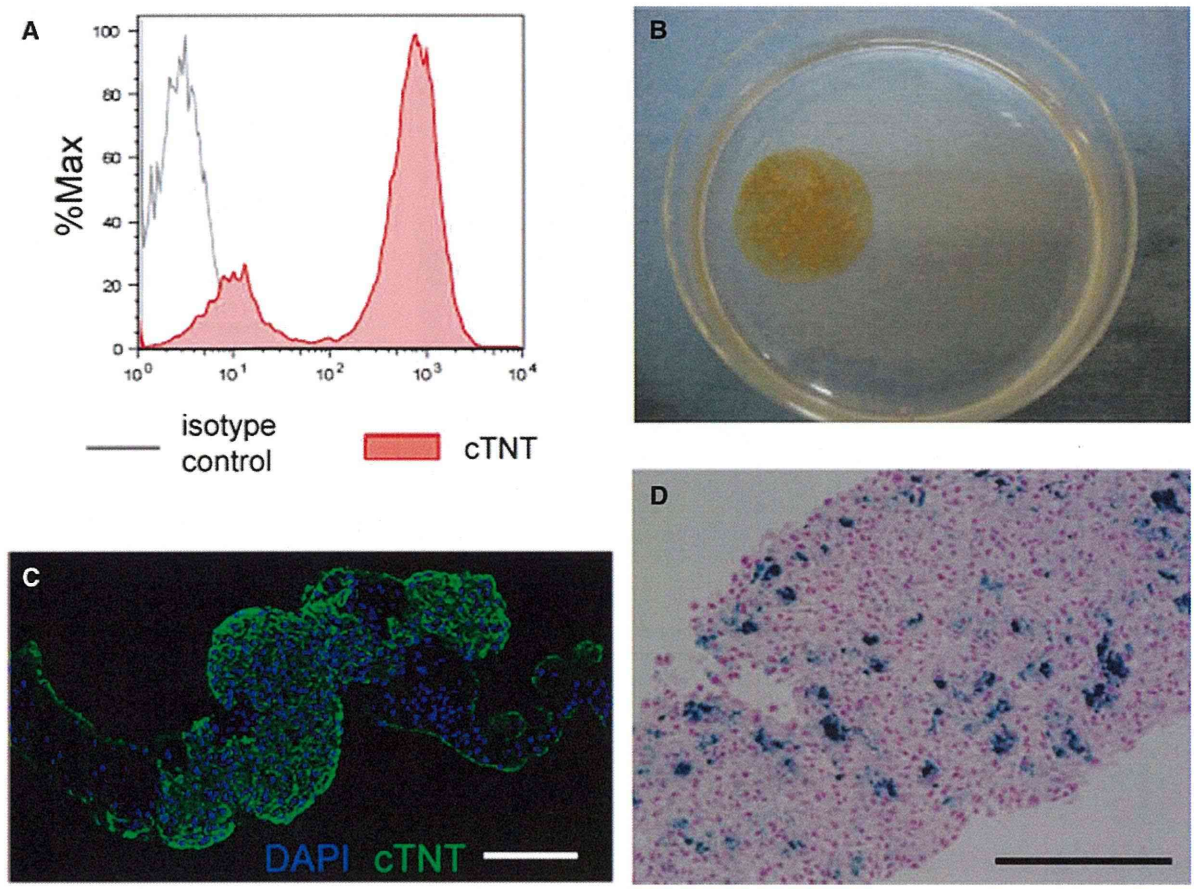

Figure 2. Histological characteristics of the human induced pluripotent stem cell–derived cardiomyocyte (hiPS-CM) cell sheet. **A**, Expression of cardiac troponin T (cTNT) after differentiation and purification of hiPS-CMs. **B**, A superparamagnetic iron oxide (SPIO)–labeled hiPS-CM cell sheet in a 10-cm dish. **C**, Immunostaining of the hiPS-CM cell sheet with cTNT antibody (green). The cell nuclei were counterstained with 4′,6-diamidino-2-phenylindole (DAPI; blue). **D**, Prussian blue staining of the SPIO-labeled hiPS-CM cell sheet. Scale bar, 50 μm in **C** and **D**.

pedicle omentum were attached over the epicardium of the left ventricle without any histological gaps in all mini-pigs, as assessed by hematoxylin–eosin staining (Figure 4D). The hearts without the omentum showed cellular and fibrous components over the anterior wall of the ventricles (Figure 4A), whereas the hearts with the omentum showed thick cellular, fibrous, and fat-rich components covering the anterior and lateral wall of the ventricles (Figure 4D).

Prussian blue staining revealed cells containing iron on the surface of the ventricles, corresponding to the area seen on CMR in both groups (Figure 4B and 4E). A larger number of cells with iron contents were identified in mini-pigs with the omentum compared with those without (Figure 4B, 4C, 4E, and 4F). In fact, the density of iron-containing cells in the transplanted site, assessed semiquantitatively by Prussian blue staining at 8 weeks after treatment, was significantly greater in the mini-pig with the omentum (27±6 cells/high-power field) than in those without it (5±2 cells/high-power field; $P<0.0001$; Figure 4G). Immunohistolabeling showed that a larger number of cells are positive for cTNT in the area where cells with iron inclusions are present in mini-pigs with the omentum compared with those without it (Figure 4H). The distribution of the SPIO particles was visualized by differential interference contrast of confocal microscopy. Grafted hiPS-CMs were identified and confirmed as double-positive for cTNT and SPIO and negative for CD68, which is a specific marker for macrophages, by immunohistolabeling (Figure 4I–4N). In addition, no teratomas were formed in the heart or other thoracic organs at 8 weeks after the transplantation of the hiPS-CM cell sheets with or without the omentum (data not shown).

Capillary Density in the Transplanted Area

Vessels and capillaries in the transplanted cell sheets at 8 weeks after transplantation were visualized and assessed by immunohistochemistry for von Willebrand factor. The transplanted cell sheets without the omentum contained a large number of capillaries and a small number of vessels in a homogeneous manner (Figure 5A), suggesting that vascular network was created possibly to support the survival and function of the cell sheets. Of note, the number of capillaries and vessels were markedly greater in the cell sheets covered by the omentum compared with those without it (Figure 5B). In fact, capillary density in the transplanted cell sheets, assessed semiquantitatively by immunohistochemistry for von Willebrand factor at 8 weeks after treatment, was significantly and markedly